Significance of Coulomb interaction in interlayer coupling, polarized Raman intensities, and infrared activities in the layered van der Waals semiconductor GaSe

Manish K. Niranjan*
Department of Physics, Indian Institute of Technology, Hyderabad 502285, India

(Received 1 January 2021; revised 2 May 2021; accepted 4 May 2021; published 26 May 2021)

Two-dimensional (2D) layered III–VI semiconductors such as GaSe have attracted a lot of attention in recent years. Bulk GaSe consists of stacks of layers held together by weak interlayer interaction generally assumed to be of van der Waals type. However, proper justification of this assumption has been lacking in the reported studies. In this paper, we explore in detail the interlayer coupling in GaSe by studying lattice dynamics using first-principles density functional theory. Our study strongly suggests that contrary to common assumption, the contribution of Coulomb interaction in interlayer coupling can be significantly higher than that of van der Waals interaction in GaSe and other similar 2D layered semiconductors. The suggested predominance of electrostatic over van der Waals interaction in interlayer coupling may have important implications for various physical properties of GaSe and related layered semiconductors. Further, we study polarized Raman spectra, infrared (IR) activities, mode symmetry assignments, and Born-effective charge tensors for bulk GaSe polytypes (β, ε, γ). The Raman mode intensities are calculated for different light polarization setups and signature Raman and IR active modes are identified for each GaSe polytype (structure). In addition, the influence of film thickness and strain on Raman and IR mode frequencies and intensities of GaSe are explored and compared with available experiments.

DOI: 10.1103/PhysRevB.103.195437

I. INTRODUCTION

The discovery of graphene and its remarkable properties have generated tremendous interest in two-dimensional (2D) layered van der Waals (vdW) semiconductors in the last decade [1–9]. In particular, 2D layered III–VI semiconductors in the MX (M = Ga, In and X = S, Se, Te) family have been found highly promising for the applications in optoelectronic, photovoltaic, nonlinear optical and terahertz (THz) generation devices [10–18]. Atomically thin GaSe nanosheets prepared by exfoliation have been found as a promising material for high performance photodetectors [10]. Recently, the transport characteristics of field effect transistor (FET) based on a single sheet of GaSe and GaS have been demonstrated [19]. The van der Waals heterostructures of GaSe with other 2D systems such as graphene, InSe, etc., have also attracted a lot of attention as these can be exploited to fabricate devices with tunable optoelectronic properties with enhanced functionalities [12,13,20–22]. Furthermore, direct epitaxy of vdW heterostructures has been suggested to be ideal for clean interlayer interfaces and scalable device fabrication [14].

The crystal structure of bulk GaSe consists of stacks of layers held together by weak interlayer coupling. In general, the layered compounds consist of structurally identical layers held together by highly anisotropic bonding forces. The forces between the layers are quite weak as compared to forces within the layers. In most of the reported studies, the weak interlayer forces have generally been assumed to be of van der Waals (vdW) type. However, this has been a common assumption and no proper justification has been provided in reported studies to the best of our knowledge. Nevertheless, it has also been suggested that the interlayer interaction in GaSe may contain an ionic or Coulomb contribution [23]. The proper understanding of interlayer forces in GaSe and other related III–VI layered semiconductors is important since various physical properties are critically influenced by the coupling between the layers. Therefore, in this paper, we carry out a detailed study of the relative contribution of Coulomb (electrostatic) and van der Waals interaction between the layers in bulk GaSe using first-principles density functional theory. The presented results strongly suggest that the Coulomb interaction may indeed play a predominant role in coupling between the layers. Furthermore, contrary to the common assumption, the contribution of the interlayer Coulomb interaction may be significantly higher than that of van der Waals interaction.

The bulk GaSe has been reported to exist in different polytypes or structures (such as β, ε, γ) with global hexagonal symmetry. These polytypes differ from each other depending on the way GaSe layers stack on top of each other [23–26]. In principle, GaSe polytypes may be identified using powerful nondestructive characterization tools such as Raman and/or infrared (IR) spectroscopy which have been widely used to study dynamical and structural properties in material systems [27,28]. Over the years, several studies of identification of stacking sequence (polytypism) in few-layer graphene and MoS_2 using Raman spectroscopy in the low-frequency range have been reported [29–32]. Recently Lim *et al.* [16] have reported a study of identification of stacking sequences for trilayer GaSe using low-frequency (below $\sim$20 cm^{-1}) Raman

*manish@phy.iith.ac.in

spectra. However, it may be noted that the identification of stacking sequences (polytypism) in bulk phases or thick samples using low-frequency Raman spectra can be extremely challenging.

Over the years, several experimental Raman and few IR studies of the GaSe system have been reported due to its technological importance. However, to best of our knowledge, no comprehensive polarized Raman and IR studies of the aforementioned bulk GaSe polytypes (β, ε, γ) and few-layer GaSe have been reported [33]. Theoretical Raman and IR studies are particularly important and offer advantage as these can be used (1) to assign symmetry labels to Raman, IR, as well as silent modes, and (2) to identify the signature Raman and/or IR active modes which may be unique to bulk GaSe polytypes (β, ε, γ) and few-layer GaSe. It may be noted that using experimental data, the symmetry assignment to all the modes for bulk structures (polytypes) may be quite challenging since the samples often may contain a mixture of more than one polytype in different proportions. Theoretical studies can also be used to systematically explore the intrinsic variation (blueshift and/or redshift) of Raman and IR mode frequencies and intensities as a function of film thickness and other factors such as strain (uniaxial, biaxial), doping, external field, etc. [27,28,34,35]. Therefore, in this paper, we also perform a detailed comprehensive first-principles theoretical study of (1) Polarized Raman and IR spectra as well as mode symmetry assignments for bulk GaSe polytypes (β, ε, γ), (2) variation of mode frequencies and intensities as a function of number of layers of ultrathin GaSe films, and (3) variation of mode frequencies and intensities of single layer (1L) GaSe due to strain. The polarized Raman spectra are obtained for different polarization directions of incoming and scattered light. The results presented in this study may be expected to serve as reference first-principles theoretical results for comparison with available experimental data and for further analyses.

The remainder of this paper is organized as follows. The theoretical and computational methodology are presented in Sec. II. The crystal and electronic structures of bulk β-, ε-, γ-GaSe are reviewed in Sec. III A. The nature of interlayer coupling is discussed in Sec. III B. The polarized Raman and IR spectra of bulk β-, ε-, γ-GaSe are presented in Sec. III C. The influence of strain and thickness on Raman and IR modes/intensities of few-layer GaSe are presented in Secs. III D and III E. Finally, the conclusions are presented in Sec. IV.

II. THEORETICAL DETAILS

A. Computational methodology

The first-principles calculations are performed within the framework of density functional theory (DFT) [36] and density functional perturbation theory (DFPT) as implemented in the VASP package [37]. The interaction between core and valence electrons is approximated using the projected augmented wave (PAW) method [38]. The Kohn-Sham single-particle orbitals are expanded using a plane wave basis set with a kinetic energy cutoff of 500 eV or higher. The local density approximation (LDA) is used to describe exchange-correlation (xc) interactions [39]. In addition, the results are also compared with those obtained using xc approximations such as PBE [40], PBEsol [41], mBJ (meta-GGA) [42] and HSE06 [43]. The interlayer van der Waals interactions are included using dispersion interaction based DFT + D3 scheme [44]. The Brillouin zones of bulk GaSe is sampled using Monkhorst-Pack $16 \times 6 \times 4$ k meshes or higher. Self-consistency in the calculations is achieved by allowing the total energies to converge up to 10^{-8} eV/cell. The atomic coordinates and lattice parameters are relaxed until the largest force on each atom is reduced to less than 0.001 eV/Å. The single- and few-layer GaSe films are simulated using a periodic slab geometry with ∼20–50-Å vacuum region. The 2D Brillouin zones of slabs are sampled using Monkhorst-Pack $16 \times 16 \times 1$ k meshes. The parameters such as zone-center phonon frequencies, dielectric permittivity tensors, Born-effective charge tensors, etc., are calculated using the linear response scheme with the iterative Green's function approach for density functional perturbation theory [37]. The Raman mode intensities are calculated from the dynamical matrices and derivatives of the dielectric constant tensors [37,45]. The phonon frequencies and eigenvectors are computed following the diagonalization of the dynamical matrices constructed from the Hellmann-Feynman forces in the unit cell. The dynamical matrices are computed for both positive and negative atomic displacements (0.01 Å). The dielectric tensors are computed using density functional perturbation theory for both positive and negative atomic displacements in the unit cell. The derivatives of the dielectric constant tensors are calculated using the finite difference approach.

B. Raman tensors and intensities

The Raman intensity spectra are calculated using the Placzeck scheme [46]. In this scheme the first-order nonresonant Stokes differential Raman cross section for the mth phonon mode can be expressed as [27,46–49]

$$I_m^R \propto \frac{d\sigma_m}{d\Omega} = N\frac{\upsilon_s^4}{c^4 V}|\vec{e}_s \cdot \overleftrightarrow{A}_m \cdot \vec{e}_i|^2 \frac{\hbar}{2\upsilon_m}\left(n_m^b + 1\right), \qquad (1)$$

where υ_m is the frequency of the mth phonon mode of the crystal; υ_i and υ_s are the the frequencies of the incoming and the scattered light, respectively. $\vec{e}_i$ ($\vec{e}_s$) is the polarization or unit vector of the electric-field direction for the incident (scattered) light. $n_m^b = (e^{h\upsilon_m/k_B T} - 1)^{-1}$ is the Bose-Einstein statistical factor for the mth phonon mode. V, N, and c are the volume of the primitive unit cell, number of primitive unit cells in the sample, and the speed of light, respectively. The frequencies of incident and scattered light are related as $\upsilon_s = \upsilon_i \pm \upsilon_m$ due to energy conservation. $\overleftrightarrow{A}_m$ is the symmetric (3×3) tensor for the mth phonon mode and can be evaluated as

$$A_{m,ij} = \frac{V}{4\pi}\sum_{\tau,\alpha}\frac{\partial \varepsilon_{ij}^{\infty}}{\partial r_{\tau\alpha}}\frac{U_m(\tau\alpha)}{\sqrt{M_\tau}}, \qquad (2)$$

where $\vec{\varepsilon}^{\infty}$ is the electronic permittivity tensor, $r_{\tau\alpha}$ is the displacement of the τth atom in the α direction, M_τ is the mass of atom τ, and $U_m(\tau\alpha)$ is the orthonormal vibrational eigenvector of the mth mode. Finally, using the Lorentzian

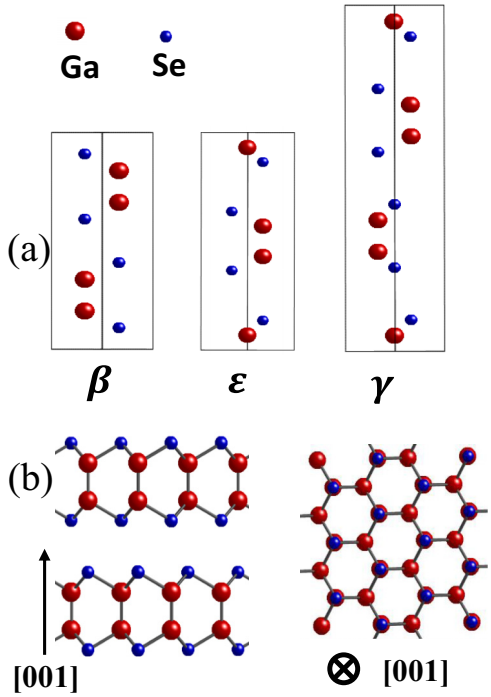

FIG. 1. (a) The hexagonal unit cells of bulk β-, ε-, and γ-GaSe. (b) Side and top view of bulk β-GaSe. The bigger red and smaller blue balls are Ga cations and Se anions respectively.

line shape and Γ_m as damping coefficient of the mth mode, the Raman intensity spectrum can be computed as

$$I(\upsilon) = \sum_m I_m \frac{\Gamma_m}{(\upsilon - \upsilon_m)^2 + \Gamma_m^2}. \tag{3}$$

In our calculations, we have used $\lambda_i = 532$ nm, $T = 300$ K, and $\Gamma_m = 2\ \mathrm{cm}^{-1}$.

C. Infrared intensities

The Infrared intensity associated with the mth phonon mode can be expressed as [50–52]

$$I_m^{\mathrm{IR}} = \sum_\alpha \left| \sum_{\tau,\beta} Z^*_{\tau,\alpha\beta} U_m(\tau\beta) \right|^2, \tag{4}$$

where $\overleftrightarrow{Z}^*_\tau$ is the Born-effective charge tensor of atom τ and $U_m(\tau\beta)$ is the eigenvector of the mth mode. The IR intensity spectrum can be obtained using an appropriate Lorentzian line shape as given in Eq. (3).

III. RESULTS AND DISCUSSION

A. Crystal and electronic structure

In this section, we briefly review the crystal and electronic structures of bulk GaSe. As shown in Fig. 1, the bulk GaSe crystal structure consists of stacks of layers held together by weak interlayer coupling. It is usually assumed that the weak forces between the layers are primarily contributed by the van der Waals interactions and possibly by minor Coulomb interactions. However, as mentioned earlier in Sec. I, no proper justification for this assumption has been reported to the best of our knowledge. Each GaSe single layer itself consists of covalently bonded four atomic layers in the Se-Ga-Ga-Se sequence. The Ga cation is bonded to another similar Ga and to three Se anions in the tetrahedral coordination. The Se anions are placed in a hexagonal arrangement at two surfaces. Further, each Se anion is bonded to three Ga cations below within the layer (See Fig. 1). The Ga cations and Se anions have coordination numbers 4 and 3, respectively. Over the years, different polytypes (β, ε, γ) of GaSe having global hexagonal symmetry have been reported [24]. These polytypes differ in the way the Se-Ga-Ga-Se layers stack on top of each other. The structures of β- and ε-GaSe have two-layer hexagonal stacking sequences. Likewise, the γ-GaSe structure has a three-layer hexagonal stacking sequence. In principle, an infinite number of stacking sequences are possible, provided that an anion is never in the same site with its closest cation nor with the adjacent-layer anion. Figure 1(a) shows the unit cells of bulk β-, ε-, γ-GaSe. As can be seen, the unit cells are similar in projection onto the hexagonal plane but differ in the number and lateral placement of stacked double layers. Figure 1(b) shows the side and top views of the bulk β-GaSe. The γ-GaSe unit cell is shown in the hexagonal setting in Fig. 1(a), though its primitive cell is rhombohedral. Table S-1 of the Supplemental Material [53] shows the space groups and Wyckoff positions of three GaSe structures. The lattice parameters and atomic positions of relaxed unit cells of β-, ε-, γ-GaSe computed using LDA, PBE, PBEsol, PBE+D3, and PBEsol+D3 schemes are listed in Tables S-2–S-4 [53], respectively. As can be seen, the lattice parameters and atomic positions computed using LDA are in reasonably good agreement with the experiments. Recently, using different xc functionals, Srour *et al.* [54] have reported a detailed comparative study of optimized crystal parameters and electronic structure of GaSe polytypes. In their study, it was suggested that the PBEsol xc scheme can be expected to perform reasonably well without any additional inclusion of the dispersion interactions (DIs). On the contrary, the combination of PBEsol with the D3 and also with D3(BJ) schemes tend to overbind, which results in underestimation of a and c (∼1–2%) lattice parameters [54]. However, as can be seen in Table S-2 [53], the LDA approximation also performs reasonably well without any additional inclusion of dispersion interactions (DIs) such as DFT-D3. Furthermore, the LDA functional has been found to provide excellent description of other well-known 2D systems such as MoS_2, WS_2 [55,56], h-BN [57], graphene/h-BN heterostructures [58]. Therefore, in the present study, we have chosen LDA to study Raman intensities of GaSe for different light polarization setups.

The band structure of bulk β-GaSe along the high symmetry directions in the Brillouin zone is shown in Fig. S-1 [53]. The band structures for 1L and 2L of GaSe films are also shown in Fig. S-1 [53]. As expected, the main features in electronic structures of bulk as well few-layer GaSe are due to hybridization between orbitals of Ga and Se atoms within the layer. The valence band is primarily comprised of Ga-4p and Se-4p orbitals. The bands at ∼14 eV and ∼7 eV below the valence band maximum (VBM) are primarily contributed by Se-4s and Ga-4s orbitals respectively. For the bulk β-GaSe, the VBM and conduction band minimum (CBM) are at Γ and

M point respectively. The band gap for the bulk β-GaSe is found to be indirect with magnitude ∼0.87 eV (LDA). The direct band gap with VBM and CBM at the Γ point is found to be ∼0.90 eV (LDA). As expected, the band gaps computed using LDA and/or GGA are underestimated as compared to the experimental GaSe band gap of ∼2.1 eV [59,60]. The band gaps computed using mBJ (meta-GGA) and HSE06 *xc* functionals are found to be 1.87 and 2.02 eV, respectively, and are in reasonable agreement with the experiments. The band gaps computed using PBE, PBE+D3, PBEsol, PBEsol+D3 are also listed in Tables S-1–S-3 [53]. The variation of band gap with increasing number of layers in GaSe films is shown in Fig. S-2 [53]. The computed band gap is highest for single layer (1L) thickness with magnitude of ∼2.2 eV (LDA), ∼3.8 eV (HSE06), ∼3.5 eV (mBJ). Further, for 1L thickness, the band gap is direct with VBM and CBM at the Γ point. The variation of GaSe band gap with increasing number of layers is consistent with that reported for similar systems such as InSe [61]. The electronic structure of ε- and γ-GaSe structures are found to be qualitatively similar to that of β-GaSe. Overall, the computed electronic structure of GaSe polytypes are consistent with those reported in earlier *ab initio* studies [54,62–64].

B. Nature of interlayer coupling in GaSe

Next, we study the lattice dynamics of bulk β-GaSe and thereby the relative contribution of electrostatic and van der Waals forces in interlayer interaction in GaSe. The β-GaSe polytype is particularly important because of the inversion center located on the midplane between layers which renders Raman and IR active modes mutually exclusive. The crystal structure of β-GaSe is hexagonal with $P6_3/mmc$ (no. 194) space group symmetry. The unit cell consists of eight atoms in two layers and each layer consists of four atoms in Se-Ga-Ga-Se sequence along [001] direction (see Fig. 1). The symmetry of the 21 optical phonon modes at the zone center (Γ point) may be classified according to the irreducible representation of D_{6h} point group as

$$\Gamma \equiv A_{2u} \oplus E_{1u} \oplus 2E_{2u} \oplus 2A_{1g} \oplus 2E_{1g} \oplus 2E_{2g} \oplus 2B_{1u} \oplus 2B_{2g}. \quad (5)$$

The Raman and IR-active modes are mutually exclusive and may be represented as

$$\text{Raman} \equiv 2A_{1g} \oplus 2E_{1g} \oplus 2E_{2g}, \quad \text{IR} \equiv A_{2u} \oplus E_{1u}. \quad (6)$$

The A_{1g} and A_{2u} modes are nondegenrate and correspond to out-of-plane (along *z* or *c* direction) atomic vibrations. On the other hand, E_{1g}, E_{2g}, and E_{1u} are doubly degenerate and corresponds to in-plane (*x*-*y* or basal plane) atomic vibrations. The rest of the modes are optically inactive (silent). The subscripts *g* and *u* indicate even (symmetric) and odd (antisymmetric) modes respectively. The computed relative directions of atomic displacements for these modes are shown in Fig. 2. Due to interlayer interaction, different layers in GaSe behave nearly isolated weakly interacting monolayers. Since there are two layers in the β-GaSe unit cell, the weak layer-layer interaction results in splitting of two degenerate normal modes (in monolayer approximation), into a pair of nondegenerate normal modes. It may be noted that in full

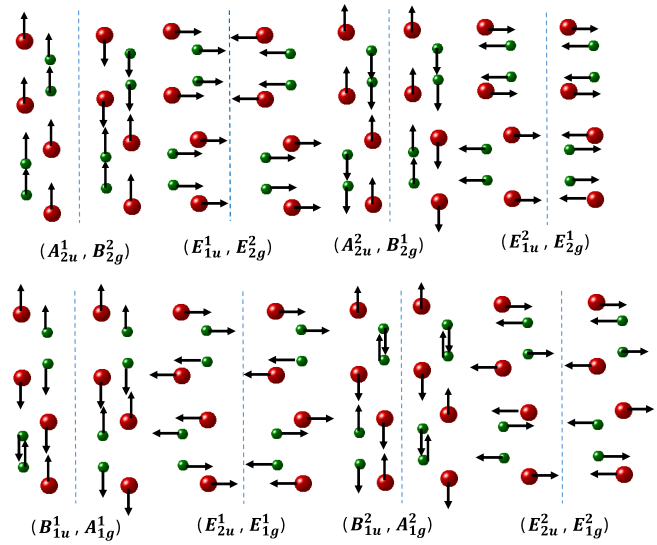

FIG. 2. The displacements of atoms in the unit cell for conjugate modes in β-GaSe. Modes in each bracket are conjugate mode pair. The bigger red and smaller green balls are Ga cations and Se anions respectively.

monolayer approximation, the interaction between the layers is assumed to vanish. The pair of monolayer modes spilt by weak interlayer interaction may be referred to as conjugate modes [23] and are shown in Fig. 2. The conjugate modes differ from each other by an interlayer phase shift of 180° due to inversion center between the layers. As can be seen in Fig. 2, for each pair of conjugate modes the vibrational displacements of the adjacent layer are out of phase in one mode and in phase in the other mode. The computed frequencies of Raman, IR, and silent modes along with their symmetry assignments are listed in Table I. As evident, the computed frequencies of most of the modes are in good agreement with the experiments [23,25,26,65]. The computed (LDA) frequencies of Raman modes of β-GaSe (with optimized cell volume) are found to be 19.2 cm^{-1} (E^2_{2g}), 57.4 cm^{-1} (E^1_{1g}), 133.4 cm^{-1} (A^1_{1g}), 210.1 cm^{-1} (E^2_{1g}), 215.2 cm^{-1} (E^1_{2g}), 309.6 cm^{-1} (A^2_{1g}). The transverse-optical (TO) IR-active mode frequencies are found to be 215.4 cm^{-1} (E^2_{1u}) and 239.3 cm^{-1} (A^2_{2u}). The degeneracy in the E^2_{1u} mode is lifted due to long-range Coulomb interaction which results in a longitudinal optical (LO) mode at ∼249.6 cm^{-1} in addition to a transverse optical (TO) mode at 215.4 cm^{-1}. The Raman mode frequencies of β-GaSe with (experimental cell volume), computed using LDA, PBE, PBEsol, PBE-D3, PBEsol-D3 are listed in Table S-5 [53]. The frequencies shown in Table I are obtained using LDA and with cell volume optimized using LDA. On the other hand, frequencies shown in Table S-5 [53] are obtained using various *xc* functionals and with cell volume fixed to experimental value. As can be seen in Table S-5 [53], the frequencies computed using PBE scheme are in better agreement with experiments as compared to those computed using LDA and PBEsol schemes. Further, the inclusion of van der Waals interaction in the PBE+D3 scheme slightly improves the accuracy of computed mode frequencies. It may be noted that excellent agreement between LDA computed frequencies shown in Table I and experimental values may

TABLE I. Frequencies (cm^{-1}) of Raman, IR, and silent modes with their symmetry assignments for bulk β-GaSe. The theoretical frequencies are computed for optimized unit cell and using LDA approximation.

	Act.	Theory	Expt.[a]	Exp.[b]	Expt.[c]	Expt.[d]
E^2_{2g}	R	19.2	19.1	20	19.5	
E^1_{1g}	R	57.4	60.1	60	60.1	59
A^1_{1g}	R	133.4	134.6	134	134.3	134
E^2_{1g}	R	210.1	249			
E^1_{2g}	R	215.2	213.1	211	214.0	213
A^2_{1g}	R	309.6	307.8	309	308.0	308
E^2_{1u}	I (TO)	215.4	213.9			
	I (LO)	249.6		250	252.1	
A^2_{2u}	I	239.3	237			
B^2_{2g}	…	36.5				
E^1_{2u}	…	55.0				
B^1_{1u}	…	128.5				
E^2_{2u}	…	210.2			211.9	
B^1_{2g}	…	246.1				
B^2_{1u}	…	310.2				

[a]Reference [23].
[b]Reference [25].
[c]Reference [26].
[d]Reference [10].

be partially due to the favorable frequency shift caused by the compressive strain. The LDA optimized cell volume is smaller by ∼3.3% as compared to experimental cell volume (see Table S-2 [53]). Furthermore, one may also note that computed mode frequencies correspond to temperature $T \sim 0$ K, whereas the experimental frequencies (in Tables I and III) correspond to temperature $T \sim 300$ K. A decrease in frequency of $\sim 1\,cm^{-1}$ for mode A^1_{1g} ($\sim 134\,cm^{-1}$) and $\sim 2\,cm^{-1}$ for mode A^2_{1g} ($\sim 309\,cm^{-1}$) may be expected for the temperature increase from ∼0 K to ∼300 K. However, an almost negligible frequency shift is expected for mode E^2_{2g} ($\sim 20\,cm^{-1}$) [66]. The temperature dependent frequency shift is attributed to anharmonicity arising from phonon-phonon coupling and three-phonon processes.

As can be seen in Table I, except for mode E^2_{1g}, the computed (LDA) mode frequencies and symmetry assignments are in good agreement with available experiments. It may be noted that the E^2_{1g} mode has not been reported by most of experimental Raman studies on GaSe as its intensity is likely to be very weak and broad under all conditions of excitation. The mode at $\sim 249\,cm^{-1}$ has been assigned E^2_{1g} symmetry in Ref. [23]. However, our results suggest that the mode at $\sim 250\,cm^{-1}$ is an IR-active LO mode with symmetry assignment E^2_{1u}. The frequency of the IR active LO mode is consistent with that reported in Ref. [25]. As shown in Table I, the computed frequency of the E^2_{1g} mode is $\sim 210\,cm^{-1}$. Thus, in our opinion, more experimental studies should be performed in order to conclusively establish the frequency and symmetry assignment to mode E^2_{1g} in β-GaSe.

Next, we discuss how the frequencies of the conjugate modes may shed light on the nature of interlayer interaction in GaSe. As can be seen in Fig. 2, the modes E^1_{1u} and E^2_{2g} are conjugate modes. The mode E^1_{1u} is the acoustic mode with frequency $0.0\,cm^{-1}$. The mode E^2_{2g} with frequency $\sim 19.2\,cm^{-1}$ can be identified as a rigid layer mode as it corresponds to out of phase rigid vibrations of two Se-Ga-Ga-Se layers with respect to each other. The frequency of the E^2_{2g} mode computed using LDA without any inclusion of van der Waals interaction is in excellent agreement with the experiments. The frequencies and atomic displacements of conjugate modes in which interlayer coupling plays the dominant role suggest that forces between layers in GaSe may not be exclusively of van der Waals type [23]. This may be understood as follows. Figure 2 shows that (E^1_{1u}, E^2_{2g}) as well as (E^2_{1u}, E^1_{2g}) are conjugate mode pairs. If the forces between the GaSe layers are assumed to be of van der Waals type only, then the frequency of the mode with out-of-phase vibration will always be higher than the frequency of the conjugate mode with in-phase vibration. This is due to the fact that the frequency is not affected by the van der Waals interaction as two layers vibrate in phase. On the other hand, the frequency is raised due to van der Waals interaction as the layers vibrate out of phase. Thus, the frequencies of the E^1_{1u} and E^2_{1u} modes are expected to be lower than those of the conjugate E^2_{2g} and E^1_{2g} modes respectively. The increment in the frequency of the E^1_{2g} mode as compared to that of the E^2_{1u} mode may be estimated using a simple model for identical coupled oscillators. In the case of two identical coupled oscillators, the frequencies are given as ω_0 and $\sqrt{\omega_0^2 + \Delta\omega_0^2}$, where ω_0 is the frequency of the isolated oscillator and represents the mode in which the oscillators vibrate in phase, with no influence of the coupling force constant on the mode frequency. Here $\Delta\omega_0$ indicates the coupling frequency which depends on the mass of the oscillators and the coupling constant. The mode frequency is $\sqrt{\omega_0^2 + \Delta\omega_0^2}$ when oscillators vibrate 180° out of phase. In the case of β-GaSe, the conjugate modes E^1_{1u} and E^2_{2g} have frequencies 0.0 and $19.2\,cm^{-1}$. Therefore, the coupling frequency is expected to be around $\Delta\omega_0 \sim 19\,cm^{-1}$. In the case of the conjugate modes E^1_{2g} and E^2_{1u}, the frequency of the E^1_{2g} mode is expected to be higher by $\sqrt{\omega_0^2 + \Delta\omega_0^2} - \omega_0 = 0.85\,cm^{-1}$ where $\omega_0 = 215.4\,cm^{-1}$ is the frequency of the antisymmetric E^2_{1u} mode. In the case of the (E^1_{1u}, E^2_{2g}) conjugate mode pair, the computed as well as experimental frequency of E^1_{1u} is lower than that of the E^2_{2g} mode as expected. However, in the case of the (E^2_{1u}, E^1_{2g}) conjugate mode pair, the computed and experimental frequency of E^2_{1u} is higher than that of the E^1_{2g} mode. This indicates that the forces between the layers may not be exclusively of van der Waals type and therefore may include a contribution from electrostatic interaction. As mentioned earlier, the frequency of the rigid layer E^2_{2g} mode computed using LDA (as well as PBE) without any extra inclusion of van der Waals interaction is found to be in good agreement with reported experimental values. The mode frequencies are improved only marginally when van der Waals interactions are included through the PBE+D3 scheme (see Table S-5 [53]). These results suggest that contrary to common assumption, the weak interaction between the layers is predominantly of

TABLE II. Diagonal components of electronic dielectric constant and Born effective charge tensor for bulk β-GaSe and ε-GaSe.

	β-GaSe			ε-GaSe	
	Theory	Expt.[a]	Expt.[b]	Theory	Expt.[c]
$\varepsilon^{\infty}_{x/y}$	8.4		8.4	8.5	7.3
ε^{∞}_{z}	7.1	6.73	7.1	7.3	
$\varepsilon^{0}_{x/y}$	11.3		10.2	11.4	10.6
ε^{0}_{z}	7.5		7.6	7.7	
$Z^{*}_{x/y}$ (Ga)	+2.18			+2.19	
$Z^{*}_{x/y}$ (Se)	−2.18			−2.19	
Z^{*}_{z} (Ga)	+0.84			+0.87	
Z^{*}_{z} (Se)	−0.84	0.74		−0.87	

[a]Reference [23].
[b]Reference [65].
[c]Reference [25].

long-range electrostatic (Coulomb) type instead of van der Waals interaction.

The computed diagonal components of Born-effective charge tensors listed in Table II further supports the view that the contribution of electrostatic interaction in interlayer coupling may be significantly higher than that of van der Waals interaction. The Born-effective charge tensor is found to be quite anisotropic with zero off-diagonal components due to symmetry. The xx, yy, and zz components of effective charges of Ga (Se) ions are found to be $+2.18e$ ($-2.18e$), $+2.18e$ ($-2.18e$), $+0.84e$ ($-0.84e$) respectively. It may be noted that the component of effective charge tensor of Se along the z direction (c axis) is $-0.84e$ and thus nonvanishing. The reasonably significant magnitude of the zz component of Born charges of Se atoms, i.e., Z^{*}_{zz}(Se), further suggests that electrostatic interaction between successive Se-Ga-Ga-Se layers in GaSe may be significantly large as compared to van der Waals interaction. The computed value of Z^{*}_{zz}(Se) is also in qualitative agreement with the experimental value obtained on the basis of IR reflectively data [23].

C. Polarized Raman intensities and IR activities

Next, we study Raman tensors, polarized Raman intensities (for different polarization setups of incident/scattered light), and IR intensities for bulk β-, ε-, γ-GaSe, and ultrathin films (few layers) of GaSe.

1. Bulk β-GaSe

The Raman tensors associated with the vibrational modes of β-GaSe are

$$A_{1g}=\begin{pmatrix} a & \cdot & \cdot \\ \cdot & a & \cdot \\ \cdot & \cdot & b \end{pmatrix};\quad E_{1g}=\begin{pmatrix} \cdot & \cdot & \cdot \\ \cdot & \cdot & c \\ \cdot & c & \cdot \end{pmatrix};$$

$$E_{1g}=\begin{pmatrix} \cdot & \cdot & -c \\ \cdot & \cdot & \cdot \\ -c & \cdot & \cdot \end{pmatrix};\quad E_{2g}=\begin{pmatrix} d & \cdot & \cdot \\ \cdot & -d & \cdot \\ \cdot & \cdot & \cdot \end{pmatrix};$$

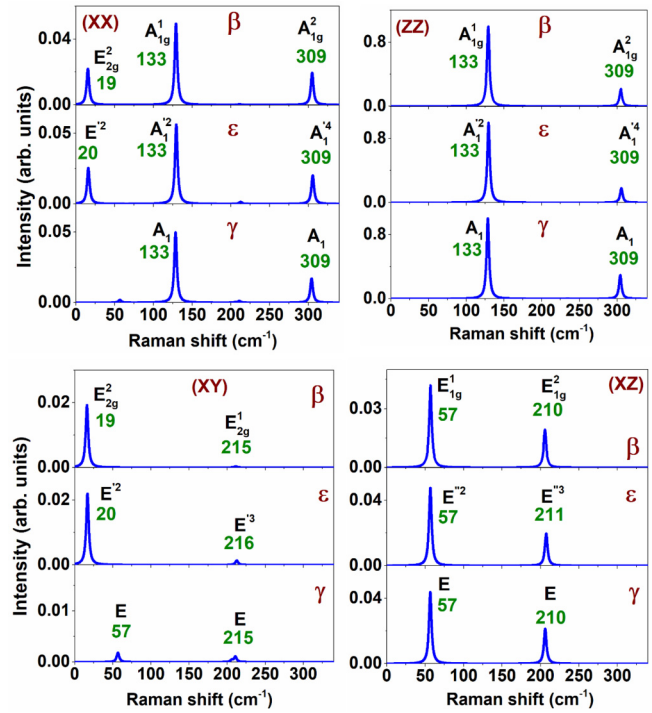

FIG. 3. The intensities of Raman active modes of bulk β-, ε-, and γ-GaSe in (XX), (ZZ), (XY), and (XZ) polarization setup.

$$E_{2g}=\begin{pmatrix} \cdot & -d & \cdot \\ -d & \cdot & \cdot \\ \cdot & \cdot & \cdot \end{pmatrix}. \tag{7}$$

Due to the symmetry of Raman tensors, the intensities of different Raman-active modes are expected to be sensitive to the polarization of incident and scattered light [see Eq. (1)]. The computed Raman intensity spectra for the $(\vec{e}_i, \vec{e}_s)$ polarization setup is shown in Fig. 3. Here $\vec{e}_i$ and $\vec{e}_s$ are the polarization direction of incident and scattered laser light. The strongest Raman intensity is obtained for mode $\sim$133 cm^{-1} (A^1_{1g}) followed by for mode $\sim$309 cm^{-1} (A^2_{1g}). As can be seen in Fig. 2, these modes are associated with the atomic vibrations along [001] or the z direction. Further, as expected, the Raman intensities of two A_{1g} modes are nonzero only for (ZZ), $(XX)/(YY)$ polarization setups. The E^2_{2g} ($\sim$19 cm^{-1}) and E^1_{2g} ($\sim$ 215 cm^{-1}) modes have nonzero intensity in the (XY) polarization setup. Further, the Raman intensity of the E^1_{1g} mode is significantly smaller than that of the E^2_{2g} mode. The E^1_{1g} ($\sim$57 cm^{-1}) and E^2_{1g} ($\sim$210 cm^{-1}) modes have nonzero intensity in the (XZ) and/or (YZ) polarization setup. The computed IR intensity is shown in Fig. 4. As can be seen, the IR intensity of the A^2_{2u} mode ($\sim$239 cm^{-1}) is significantly lower than that of the E_{1u} mode ($\sim$ 215 cm^{-1}).

It may be noted that the Raman mode intensities may be quite sensitive to the angle between the polarization of incoming and scattered light [55]. As discussed in Sec. II B, the intensity of the mth Raman active mode exhibits dependence on light polarizations as $I^R_m \propto |\vec{e}_s \cdot \overleftrightarrow{A}_m \cdot \vec{e}_i|^2$. In the case of (XX) and (ZZ) setups, the polarization vectors are given as $\vec{e}_i = \vec{e}_s = (1, 0, 0)$ and $\vec{e}_i = \vec{e}_s = (0, 0, 1)$ respectively. However, for polarizations in the x−z plane and $\vec{e}_i =$

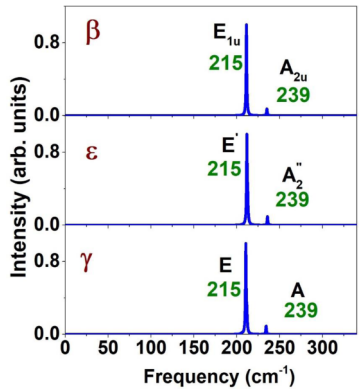

FIG. 4. The intensities of Infrared (IR) active modes of bulk β-, ε-, and γ-GaSe.

$\vec{e}_s = [\cos(\theta), 0, \sin(\theta)]$, the intensity for A_{1g} modes is given as $I(A_{1g}) \propto |(a\text{-}b)cos^2(\theta) + b|^2$. Thus, the intensity of the A_{1g} mode varies from a^2 to b^2 with the angle between the polarization changing from 0 ° to 90 ° in the $x-z$ plane. The E_{1g} modes have nonzero Raman intensities only for polarization directions in the x-z and/or y-z planes. Thus, polarizations in the x-z plane with $\vec{e}_i = (1, 0, 0)$ and $\vec{e}_s = [\cos(\theta), 0, \sin(\theta)]$, the intensity is given as $I(E_{1g}) \propto c^2\sin^2(\theta)$. The intensity $I(E_{1g})$ varies from 0 to c^2 as the angle between the polarizations in the x-z plane is varied from 0 ° to 90 °. The Raman intensities of the E_{2g} modes are nonzero only for polarization directions in the x-y plane. Therefore, for polarizations in the x-y plane with $\vec{e}_i = (1, 0, 0)$ and $\vec{e}_s = [\cos(\theta), \sin(\theta), 0]$, the intensity is given as $I(E_{2g}) \propto d^2\sin^2(\theta)$ which varies from 0 to d^2 as the angle between the polarizations in the x-y plane is varied from 0 ° to 90 °. These results suggest that different experimental studies may report disparate Raman intensities due to difference in polarization setups which may arise as different samples may consist of different crystal orientations.

It may also be noted that different incident laser frequencies are used in different experimental setups. However, the change in intensity ratios due to the change in incident laser frequency is insignificant since intensities of all Raman modes are affected identically by incident laser frequency.

2. Bulk ε-GaSe

The crystal structure of bulk ε-GaSe is hexagonal with space group symmetry $P\text{-}6m_2/mmc$ (no. 187). As shown in Fig. 1, the unit cell consists of eight atoms in two layers. Each Se-Ga-Ga-Se layer is similar to that in β-GaSe and consists of a single plane of selenium atoms on either side of double planes of gallium atoms. The 21 optical phonon modes at the zone center (Γ point) may be classified according to the irreducible representation of the D_{3h} point group as

$$\Gamma \equiv 4A_1' \oplus 3A_2'' \oplus 3E' \oplus 4E''. \tag{8}$$

The ε-GaSe structure has no inversion center unlike that in β-GaSe. This results in some of the modes being both Raman as well as IR active. The Raman and IR-active modes are

$$\begin{aligned} \text{IR} &\equiv 3A_2'' \oplus 3E'; \\ \text{Raman} &\equiv 4A_1' \oplus 3E' \oplus 4E''; \\ \text{IR} + \text{Raman} &\equiv 3E'. \end{aligned} \tag{9}$$

TABLE III. Frequencies of Raman, IR, and silent modes with their symmetry assignments for bulk ε-GaSe.

	Act.	Theory	Expt.[a]	Expt.[b]	Expt.[c]	Expt.[d]
$E'^2(E^2_{2g})$	R+I	20.2	20	19.5		
$A_2''^2(B^2_{2g})$	I	35.1				
$E''^1(E^1_{2u})$	R	54.8				
$E''^2(E^1_{1g})$	R	57.2	60	60.1	59	
$A_1'^1$ (B^1_{1u})	R	128.4				
$A_1'^2$ (A^1_{1g})	R	133.4	134	134.3	134	135.7
$E''^4(E^2_{1g})$	R	209.5				
$E''^3(E^2_{2u})$	R	211.2		211.9		
E'^4 (E^1_{2g})	R+I (TO)	214.9	211	214.0	213	214.5
E'^3 (E^2_{1u})	R+I (TO)	216				
	R+I (LO)	249.1	250	252.1	250	
$A_2''^3(A^2_{2u})$	I	238.6				
$A_2''^4(B^1_{2g})$	I	245.7			245	
$A_1'^4(A^2_{1g})$	R	309.3	309	308.0	308	308.8
$A_1'^3(B^2_{1u})$	R	309.9				

[a]Reference [25].
[b]Reference [26].
[c]Reference [16].
[d]Reference [20].

The A_1' and A_2'' modes are nondegenerate and correspond to atomic vibrations along the [001] or c direction. The E' and E'' modes are doubly degenerate and are associated to in-plane (x-y or basal plane) atomic vibrations. The E' modes are both Raman and IR active. It may be noted that there are no silent modes in ε-GaSe unlike those present in β-GaSe. The computed (LDA) Raman and IR active modes with their symmetry assignments are listed in Table III. The correspondence between modes of ε-GaSe and β-GaSe is also shown in Table III. As can be seen, the computed Raman and IR active modes are in good agreement with reported experimental values. The computed (LDA) Raman active modes are 20.2 cm^{-1} (E'^2), 54.8 cm^{-1} (E''^1), 57.2 cm^{-1} (E''^2), 128.4 cm^{-1} ($A_1'^1$), 133.3 cm^{-1} ($A_1'^2$), 209.5 cm^{-1} (E''^4), 211.2 cm^{-1} (E''^3), 214.8 cm^{-1} (E'^4), 216.4 cm^{-1} (E'^3), 309.3 cm^{-1} ($A_1'^4$), 309.9 cm^{-1} ($A_1'^3$). The IR-active TO modes are found to be 20.2 cm^{-1} (E'^2), 35.1 cm^{-1} ($A_2''^2$), 214.9 cm^{-1} (E'^4), 216.4 cm^{-1} (E'^3), 238.6 cm^{-1} ($A_2''^3$), 245.8 cm^{-1} ($A_2''^4$). It may be noted that in the case of ε-GaSe, though additional modes are Raman and/or IR active as compared to those in β-GaSe, intensities of some of these modes are extremely weak or even negligible as discussed later in the section. Moreover, experimental studies have reported only six Raman active (first order nonresonant) modes for ε-GaSe possibly due to negligible intensities of other Raman and/or IR modes. As can be seen in Table II, the computed frequencies of Raman and IR active modes are in good agreement with available experiments [16,20,25,26].

The Raman tensors associated with the Raman-active modes of ε-GaSe are

$$A'_1 = \begin{pmatrix} a & \cdot & \cdot \\ \cdot & a & \cdot \\ \cdot & \cdot & b \end{pmatrix}; \quad E'' = \begin{pmatrix} \cdot & \cdot & \cdot \\ \cdot & \cdot & c \\ \cdot & c & \cdot \end{pmatrix};$$
$$E'' = \begin{pmatrix} \cdot & \cdot & -c \\ \cdot & \cdot & \cdot \\ -c & \cdot & \cdot \end{pmatrix}, \quad E' = \begin{pmatrix} d & \cdot & \cdot \\ \cdot & -d & \cdot \\ \cdot & \cdot & \cdot \end{pmatrix};$$
$$E' = \begin{pmatrix} \cdot & -d & \cdot \\ -d & \cdot & \cdot \\ \cdot & \cdot & \cdot \end{pmatrix}. \tag{10}$$

As can be seen, the structures of Raman tensors of A'_1, E'', and E' modes are the same as those of A_{1g}, E_{1g}, and E_{2g} modes of β-GaSe. The computed Raman intensities for the $(\vec{e}_i, \vec{e}_s)$ polarization setup are shown in Fig. 3. The primary Raman-active modes at 133.3 cm^{-1} ($A_1^{'2}$) and 309.9 cm^{-1} ($A_1^{'3}$) can be seen for the (ZZ) and $(XX)/(YY)$ polarization setup. The $E^{'2}$ mode (20.2 cm^{-1}) is the rigid layer mode and is equivalent to the E^1_{2g} mode (19.2 cm^{-1}) in β-GaSe. The Raman intensity for this mode is significant for (XX) and (XY) configurations. The Raman intensity is found sizeable for the $E^{'2}$ (19.2 cm^{-1}) and $E^{'4}$ (214.9 cm^{-1}) mode in the (XY) configuration. In the case of the $(XZ)/(YZ)$ configuration, the Raman peaks for the $E^{''2}$ (56.2 cm^{-1}) and $E^{''4}$ (209.5 cm^{-1}) modes can be seen in Fig. 3. Further, the IR intensity is found to be highest for the $E^{'4}$ (214.9 cm^{-1}) TO mode (see Fig. 4). The degeneracy in the $E^{'4}$ mode is lifted due to LO-TO splitting which results in a TO mode at 214.9 cm^{-1} and a LO mode at 249.1 cm^{-1}. Both of these modes are Raman active in the case of ε-GaSe. In addition, a small IR peak for the $A_2^{''3}$ (238.6 cm^{-1}) mode can also be seen in Fig. 4. The intensities for other IR-active modes $E^{'2}$ (20.2 cm^{-1}) and $A_2^{''2}$ (35.1 cm^{-1}) are found to be relatively very weak. The components of Born effective charge tensors and electronic dielectric constants for ε-GaSe are listed in Table II and are found to be quite similar to those computed for β-GaSe.

Next, we comment on the modes which may be used to distinguish the presence of bulk β-GaSe and/or ε-GaSe in experimental samples. Figures 3 and 4 show that the Raman and IR intensities for bulk β-GaSe and/or ε-GaSe polytypes are almost identical which renders their identification quite challenging. It may be noted that in the case of few-layer samples the polytypes may be identified from analysis of Raman spectra in the low-frequency range (below ~20 cm^{-1}) as recently reported in Ref. [16] for few-layer GaSe. However, for bulk samples the identification of polytypes using low-frequency Raman modes becomes almost intractable. As can be seen in Table III, the rigid layer $E^{'2}$ mode (~20 cm^{-1}) in ε-GaSe is IR as well as Raman active, whereas the corresponding rigid layer E^2_{2g} mode in β-GaSe is only Raman active. Therefore, IR activity of this mode at ~20 cm^{-1} will clearly indicate the structure to be that of ε-GaSe. However, our results suggest that the rigid layer $E^{'2}$ mode (20 cm^{-1}) in ε-GaSe, though IR active, has almost negligible IR activity. Table I and III also show that the $E^{'3}$ (E^2_{1u}) mode with frequency ~250 cm^{-1} is an IR-active LO mode in ε-GaSe (β-GaSe). However, this mode is also Raman active in the case of ε-GaSe. Therefore, the presence (absence) of this mode (~250 cm^{-1}) in the Raman spectra can be used to confirm the structure to be that of ε-GaSe (β-GaSe). It may be noted that the computed first-order Raman activity of this mode (at ~250 cm^{-1}) is found to be very weak which may render it hard to detect in Raman experiments. Nevertheless, this mode can be detected using resonant Raman enhancement as reported in Ref. [25].

3. Bulk γ-GaSe

As shown in Fig. 1, the hexagonal γ-GaSe unit cell with *R3m* space group symmetry (no. 160) consists of three layers (Se-Ga-Ga-Se sequence) and twelve atoms (see Fig. 1). The 33 optical phonons at the zone center are both Raman and IR active and may be classified according to the irreducible representation of C_{3V} point group as

$$\Gamma \equiv 11A_1 \oplus 11E, \quad \text{Raman} + \text{IR} \equiv 11A_1 \oplus 11E. \tag{11}$$

The nondegenerate A_1 and doubly degenerate E modes correspond to out-of-plane and in-plane atomic vibrations. The computed (LDA) frequencies of the main Raman modes are 57.1 cm^{-1} (E), 133.4 cm^{-1} (A_1), 210.8 cm^{-1} (E), 215.3 cm^{-1} (E), 237.9 cm^{-1} (A_1), 308.8 cm^{-1} (A_1). The Raman tensors associated with the modes of γ-GaSe are

$$A_1 = \begin{pmatrix} a & \cdot & \cdot \\ \cdot & a & \cdot \\ \cdot & \cdot & b \end{pmatrix}; \quad E = \begin{pmatrix} \cdot & c & d \\ c & \cdot & \cdot \\ d & \cdot & \cdot \end{pmatrix};$$
$$E = \begin{pmatrix} c & \cdot & \cdot \\ \cdot & -c & d \\ \cdot & d & \cdot \end{pmatrix}. \tag{12}$$

Figure 3 shows the computed Raman intensity for the $(\vec{e}_i, \vec{e}_s)$ polarization setup. The primary Raman-active modes at 133 and 309 cm^{-1} with A_1 symmetry can be seen for the (ZZ) and $(XX)/(YY)$ polarization setups. For the (XY) setup, the Raman peaks for E modes at 57 and 215 cm^{-1} can be seen. Likewise, for the $(XZ)/(YZ)$ setup, the Raman peaks for E modes at 57 and 215 cm^{-1} can be seen. The computed IR intensity is shown in Fig. 4. Though all modes are also IR active, the IR intensity is significant for the E mode with frequency 215 cm^{-1}. In addition, a small IR peak can also be seen for the A mode at 237.9 cm^{-1}.

D. Few layers (ultrathin films) of GaSe

Next, we discuss the shifts in frequencies and intensities of Raman and IR active modes as the thickness (number of layers) of GaSe ultrathin films is increased. The computed Raman mode frequencies and intensities for 1L–6L of β-GaSe in the (XX) polarization setup are shown in Fig. 5. Here, 1L indicates a single layer with four planes in the Se-Ga-Ga-Se sequence. As can be seen, the frequency of the A^1_{1g} mode increases (blueshift) from 129.7 to 133.4 cm^{-1} as the number of layers is increased from 1L to bulk. However, the frequency of the A^2_{1g} mode decreases (redshift) from 312.6 to 309.6 cm^{-1} as the layers are increased from 1L to bulk. The change in Raman intensity of these modes as a function of layers is shown in Fig. 5(c). The Raman intensities of both A^1_{1g} and A^2_{1g} modes increase with increasing number of layers. However the relative increase in intensity is higher for mode

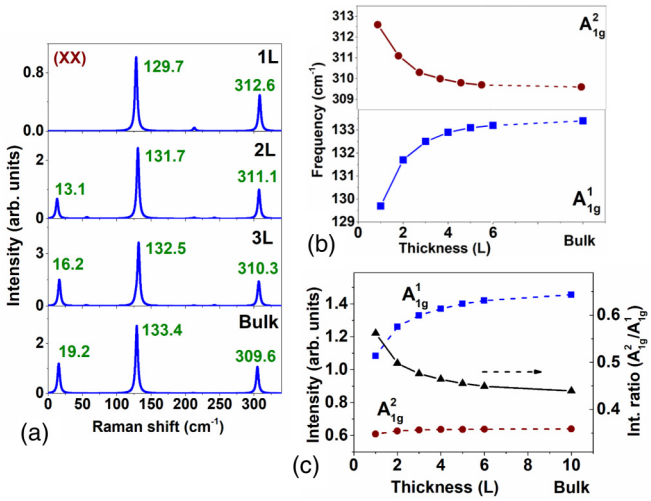

FIG. 5. (a) The Raman intensities of few-layer (1L, 2L, 3L) and bulk β-GaSe in (XX) polarization setup. (b) The frequencies of A^1_{1g} and A^2_{1g} modes. (c) The Raman intensities of A^1_{1g} and A^2_{1g} modes and intensity ratio (A^2_{1g}/A^1_{1g}) in few-layer β-GaSe with varying thickness.

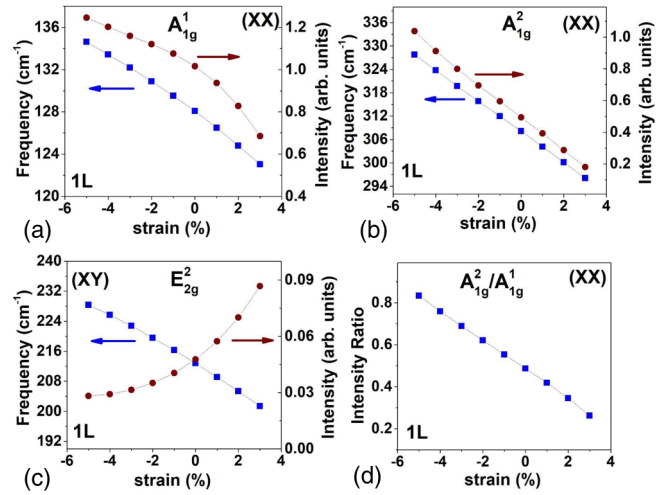

FIG. 6. The frequency of (a) A^1_{1g}, (b) A^2_{1g}, (c) E^2_{2g} modes and (d) intensity ratio (A^2_{1g}/A^1_{1g}) as function of strain in one layer (1L) thick GaSe film.

A^1_{1g} than for A^2_{1g} mode. Further, as expected, no rigid layer mode ($\sim$20 cm^{-1}) is obtained for a single layer (1L). The frequency of the rigid layer mode increases as the layers are increased from 2L to bulk. The increase in frequency of the A^1_{1g} mode ($\sim$133 cm^{-1}) with layer numbers may be attributed to the increment in interlayer interactions which results in the enhancement of the effective restoring forces acting on the atoms [55]. On the other hand, a decrease in frequency of the A^2_{1g} mode ($\sim$308 cm^{-1}) may be indicative of enhancement of dielectric screening of the long-range Coulomb forces and thereby lowering of the effective restoring force on the atoms. The enhancement in dielectric screening in the case of A^2_{1g} may be due to a larger ionic contribution as compared to that for the A^1_{1g} mode. As can be seen in Fig. 2, the Ga and Se ions in two layers vibrate out of phase in the case of the A^2_{1g} mode whereas the vibrations are in phase in the case of the A^1_{1g} mode. Overall the computed variation of frequencies of A^1_{1g} and A^1_{1g} modes with increasing number of GaSe layers is consistent with reported experiments [16].

We have also studied the variation of band gaps and electronic dielectric constants of GaSe films as the number of layers is increased (see Fig. S-2 [53]). The band gap (LDA) of few layer GaSe decreases from 2.2 to 0.87 eV as the thickness is increased from 1L to bulk. The band gap changes (increases) significantly as layers are decreased from 2L to 1L, which indicates the transition from indirect to direct band gap (see Fig. S-2 [53]). The electronic dielectric constant tensor is found to be diagonal with off-diagonal components with magnitude zero. Further, the in-plane components ε_{xx} and ε_{yy} are equal due to symmetry. The magnitudes of ε_{xx} (ε_{zz}) are increased from 3.34 (1.37) to 8.44 (7.40) respectively, as thickness is increased from 1L to bulk. The variation of band gap and dielectric constants with increasing number of layers is expected since the dielectric constant increases with decreasing band gap [55].

E. Influence of strain on Raman mode frequencies and intensities

Next, we study the shift in Raman mode frequencies and intensities due to external strain in single layer (1L) GaSe film. There are four atoms in 1L-GaSe. The symmetry of nine optical phonon modes at the zone center (Γ point) may be expressed according to the irreducible representation of the D_{3h} point group as

$$\begin{aligned} \Gamma &\equiv 2A'_1 \oplus A'_2 \oplus E' \oplus 2E'', \\ \text{Raman} &\equiv 2A'_1 \oplus E' \oplus 2E'', \\ \text{IR} &\equiv A''_2 \oplus E', \quad \text{Raman} + \text{IR} \equiv E'. \end{aligned} \tag{13}$$

In the case of relaxed 1L-GaSe, the computed frequencies of five Raman active modes are 55.3 cm^{-1} (E''), 129.7 cm^{-1} (A'_1), 211.3 cm^{-1} (E''), 216.8 cm^{-1} (E'), and 312.6 cm^{-1} (A'_1). The two IR-active TO modes are 216.8 cm^{-1} (E') and 248.5 cm^{-1} (A''_2). It may be noted that the A'_1, E'', and E' modes of 1L-GaSe correspond to the A_{1g}, E_{1g}, and E_{2g} modes of bulk β-GaSe. Figure 6 shows the variation in the frequencies and intensities of the A'^1_1 (A^1_{1g}), $A'^2_1(A^2_{1g})$, and E' (E^2_{2g}) modes as a function of compressive and tensile biaxial strain. The E' (E^2_{2g}) mode is the primary IR active mode. As expected, the mode frequencies increase almost linearly with compressive strain. The increment in the frequencies of the A'^1_1 (A^1_{1g}), $A'^2_1(A^2_{1g})$, and E' (E^2_{2g}) modes are found to be $\sim$1.4, $\sim$3.9, and $\sim$3.4 cm^{-1} respectively for 1% of compressive strain. Moreover, the Raman intensity of the A^1_{1g} and A^2_{1g} modes also increase with compressive strain. However, the increase in intensity is higher for the A^2_{1g} mode as compared to that for the A^1_{1g} mode. On the other hand, the Raman intensity decreases in the case of the E^2_{2g} mode. The variation of mode frequencies and intensities with uniaxial strain can be expected to be qualitatively similar to that found in the case of biaxial strain [55].

IV. CONCLUSION

First principles calculations are performed to investigate the contribution of Coulomb (electrostatic) and van der Waals interactions in interlayer coupling in the two-dimensional layered semiconductor GaSe. The nature of weak forces between the layers in GaSe is explored by studying the frequencies of conjugate vibrational modes and the Born effective charge tensors of ions. The computed results strongly suggest that, contrary to common assumption, the interlayer coupling in GaSe and other similar 2D layered semiconductors may be dominated by electrostatic interaction as compared to van der Waals interaction. In addition, the polarized Raman spectra, infrared (IR) activities, and mode symmetry assignments of bulk GaSe polytypes (β, ε, γ) are studied. The Raman mode intensities are calculated for different polarizations of incident/scattered laser light and signature modes are identified for each GaSe polytype (structure). The results also suggest that bulk GaSe polytypes may be quite challenging to differentiate solely from the analysis of Raman spectra. Nevertheless, the bulk phases may be identified by the combined analysis of IR and Raman spectra. The variation of Raman, IR mode frequencies, and intensities with increasing film thickness and strain are studied. The computed mode frequencies, polarized Raman, and IR spectra may be used as benchmark *ab initio* theoretical results for comparison with experiments. We hope that the results presented in this work will stimulate further theoretical and experimental studies on GaSe and related 2D layered semiconductors.

ACKNOWLEDGMENT

The author gratefully acknowledges the partial support from DST-FIST (Grant No. SR/FST/PSI-215/2016) for computational resources used in this work.

[1] Q. H. Wang, K. Kalantar-Zadeh, A. Kis, J. N. Coleman, and M. S. Strano, Electronics and optoelectronics of two-dimensional transition metal dichalcogenides, Nat. Nanotechnol. **7**, 699 (2012).

[2] R. Mas-Balleste, C. Gómez-Navarro, J. Gómez-Herrero, and F. Zamora, 2D materials: To graphene and beyond, Nanoscale **3**, 20 (2011).

[3] M. Osada and T. Sasaki, Two-dimensional dielectric nanosheets: Novel nanoelectronics from nanocrystal building blocks, Adv. Mater. **24**, 210 (2012).

[4] M. Xu, T. Liang, M. Shi, and H. Chen, Graphene-like two-dimensional materials, Chem. Rev. **113**, 3766 (2013).

[5] S. Z. Butler, S. M. Hollen, L. Cao, Y. Cui, J. A. Gupta, H. R. Gutiérrez, T. F. Heinz, S. S. Hong, J. Huang, A. F. Ismach *et al.*, Progress, challenges, and opportunities in two-dimensional materials beyond graphene, ACS Nano **7**, 2898 (2013).

[6] A. K. Geim and I. V. Grigorieva, Van der Waals heterostructures, Nature (London) **499**, 419 (2013).

[7] G. R. Bhimanapati, Z. Lin, V. Meunier, Y. Jung, J. Cha, S. Das, D. Xiao, Y. Son, M. S. Strano, V. R. Cooper *et al.*, Recent advances in two-dimensional materials beyond graphene, ACS Nano **9**, 11509 (2015).

[8] H. Fang, C. Battaglia, C. Carraro, S. Nemsak, B. Ozdol, J. Seuk Kang, H. A. Bechtel, S. B. Desai, F. Kronast, A. A. Unal *et al.*, Strong interlayer coupling in van der Waals heterostructures built from single-layer chalcogenides, Proc. Natl. Acad. Sci. USA **111**, 6198 (2014).

[9] G. Fiori, F. Bonaccorso, G. Iannaccone, T. Palacios, D. Neumaier, A. Seabaugh, S. K. Banerjee, and L. Colombo, Electronics based on two-dimensional materials, Nat. Nanotechnol. **9**, 768 (2014).

[10] P. Hu, Z. Wen, L. Wang, P. Tan, and K. Xiao, Synthesis of few-layer GaSe nanosheets for high performance photodetectors, ACS Nano **6**, 5988 (2012).

[11] S. Yang, C. Wang, C. Ataca, Y. Li, H. Chen, H. Cai, A. Suslu, J. C. Grossman, C. Jiang, Q. Liu, and S. Tongay, Self-driven photodetector and ambipolar transistor in atomically thin GaTe-MoS_2 p–n vdW heterostructure, ACS Appl. Mater. Interfaces **8**, 2533 (2016).

[12] F. Yan, L. Zhao, A. Patanè, P. Hu, X. Wei, W. Luo, D. Zhang,Q. Lv, Q. Feng, C. Shen *et al.*, Fast, multicolor photodetection with graphene-contacted p-GaSe/n-InSe van der Waals heterostructures, Nanotechnology **28**, 27LT01 (2017).

[13] Z. B. Aziza, H. Henck, D. Pierucci, M. G. Silly, E. Lhuillier, G. Patriarche, F. Sirotti, M. Eddrief, and A. Ouerghi, van der Waals epitaxy of GaSe/Graphene heterostructure: Electronic and interfacial properties, ACS Nano **10**, 9679 (2016).

[14] X. Li, L. Basile, B. Huang, C. Ma, J. Lee, I. V. Vlassiouk, A. A. Puretzky, M.-W. Lin, M. Yoon, M. Chi *et al.*, Van der Waals epitaxial growth of GaSe domains on graphene, ACS Nano **9**, 8078 (2015).

[15] H. Huang, P. Wang, Y. Gao, X. Wang, T. Lin, J. Wang, L. Liao, J. Sun, X. Meng, Z. Huang *et al.*, Highly sensitive phototransistor based on GaSe nanosheets, Appl. Phys. Lett. **107**, 143112 (2015).

[16] S. Y. Lim, J.-U. Lee, J. H. Kim, L. Liang, X. Kong, T. T. H. Nguyen, Z. Lee, S. Cho, and H. Cheong, Polytypism in few-layer gallium selenide, Nanoscale **12**, 8563 (2020).

[17] C. S. Jung, F. Shojaei, K. Park, J. Y. Oh, H. S. Im, D. M. Jang, J. Park, and H. S. Kang, Red-to-Ultraviolet emission tuning of two-dimensional Gallium Sulfide/Selenide, ACS Nano **9**, 9585 (2015).

[18] D. A. Bandurin, A. V. Tyurnina, G. L. Yu, A. Mishchenko, V. Zólyomi, S. V. Morozov, R. K. Kumar, R. V. Gorbachev, Z. R. Kudrynskyi, S. Pezzini *et al.*, High electron mobility, quantum Hall effect and anomalous optical response in atomically thin InSe, Nat. Nanotechnol. **12**, 223 (2017).

[19] D. J. Late, B. Liu, J. Luo, A. Yan, H. S. S. R. Matte, M. Grayson, C. N. R. Rao, and V. P. Dravid, GaS and GaSe ultrathin layer transistors, Adv. Mater. **24**, 3549 (2012).

[20] D. J. Terry, V. Zólyomi, M. Hamer, A. V. Tyurnina, D. G. Hopkinson, A. M. Rakowski, S. J. Magorrian, N. Clark, Y. M. Andreev, O. Kazakova *et al.*, Infrared-to-violet tunable optical

activity in atomic films of GaSe, InSe, and their heterostructures, 2D Mater. **5**, 041009 (2018).

[21] X. Li, M.-W. Lin, J. Lin, B. Huang, A. A. Puretzky, C. Ma, K. Wang, W. Zhou, S. T. Pantelides, M. Chi *et al.*, Two-dimensional GaSe/$MoSe_2$ misfit bilayer heterojunctions by van der Waals epitaxy, Sci. Adv. **2**, e1501882 (2016).

[22] M.-W. Chen, H. Kim, D. Ovchinnikov, A. Kuc, T. Heine, O. Renault, and A. Kis, Large-grain MBE-grown GaSe on GaAs with a Mexican hat-like valence band dispersion, npj 2D Mater. Appl. **2**, 2 (2018).

[23] T. J. Wieting and J. L. Verble, Interlayer bonding and the lattice vibrations of β-GaSe, Phys. Rev. B **5**, 1473 (1972).

[24] A. Kuhn, A. Chevy, and R. Chevalier, Crystal structure and interatomic distances in GaSe, Phys. Status Solidi A **31**, 469 (1975).

[25] H. Yoshida, S. Nakashima, and A. Mitsuishi, Phonon Raman spectra of layer compound GaSe, Phys. Status Solidi B **59**, 655 (1973).

[26] R. M. Hoff, J. C. Irwin, and R. M. A. Lieth, Raman Scattering in GaSe, Can. J. Phys. **53**, 1606 (1975).

[27] *Light Scattering in Solids II*, edited by M. Cardona and G. Güntherodt (Springer-Verlag, Berlin, 1982), Vol. 50.

[28] D. A. Long, *The Raman Effect: A Unified Treatment of the Theory of Raman Scattering by Molecules* (Wiley, New York, 2002).

[29] W. Na, K. Kim, J.-U. Lee, and H. Cheong, Davydov splitting and polytypism in few-layer MoS_2, 2D Materials **6**, 015004 (2018).

[30] J.-U. Lee, K. Kim, S. Han, G. H. Ryu, Z. Lee, and H. Cheong, Raman signatures of polytypism in molybdenum disulfide, ACS Nano **10**, 1948 (2016).

[31] X. Lu, M. I. B. Utama, J. Lin, X. Luo, Y. Zhao, J. Zhang, S. T. Pantelides, W. Zhou, S. Y. Quek, and Q. Xiong, Rapid and nondestructive identification of polytypism and stacking sequences in few-layer molybdenum diselenide by Raman spectroscopy, Adv. Mater. **27**, 4502 (2015).

[32] C. H. Lui, L. M. Malard, S. Kim, G. Lantz, F. E. Laverge, R. Saito, and T. F. Heinz, Observation of layer-breathing mode vibrations in few-layer graphene through combination Raman scattering, Nano Lett. **12**, 5539 (2012).

[33] X. Zhang, Q.-H. Tan, J.-B. Wu, W. Shi, and P.-H. Tan, Review on the Raman spectroscopy of different types of layered materials, Nanoscale **8**, 6435 (2016).

[34] C. Song, F. Fan, N. Xuan, S. Huang, C. Wang, G. Zhang, F. Wang, Q. Xing, Y. Lei, Z. Sun *et al.*, Drastic enhancement of the Raman intensity in few-layer InSe by uniaxial strain, Phys. Rev. B **99**, 195414 (2019).

[35] S. R. Tamalampudi, R. Sankar, H. Apostoleris, M. A. Almahri, B. Alfakes, A. Al-Hagri, R. Li, A. Gougam, I. Almansouri, M. Chiesa, and J.-Y. Lu, Thickness-dependent resonant Raman and E′ photoluminescence spectra of Indium Selenide and Indium Selenide/Graphene heterostructures, J. Phys. Chem. C **123**, 15345 (2019).

[36] W. Kohn and L. J. Sham, Self-consistent equations including exchange and correlation effects, Phys. Rev. **140**, A1133 (1965).

[37] G. Kresse and J. Furthmuller, Efficient iterative schemes for *ab initio* total energy calculations using a plane-wave basis set, Phys. Rev. B **54**, 11169 (1996).

[38] P. E. Blöchl, Projector augmented-wave method, Phys. Rev. B **50**, 17953 (1994).

[39] D. M. Ceperley and B. J. Alder, Ground State of the Electron Gas by a Stochastic Method, Phys. Rev. Lett. **45**, 566 (1980).

[40] J. P. Perdew, K. Burke, and M. Ernzerhof, Generalized Gradient Approximation Made Simple, Phys. Rev. Lett. **77**, 3865 (1996).

[41] J. P. Perdew, A. Ruzsinszky, G. I. Csonka, O. A. Vydrov, G. E. Scuseria, L. A. Constantin, X. Zhou, and K. Burke, Restoring the Density-Gradient Expansion for Exchange in Solids and Surfaces, Phys. Rev. Lett. **100**, 136406 (2008).

[42] F. Tran and P. Blaha, Accurate Band Gaps of Semiconductors and Insulators with a Semilocal Exchange-Correlation Potential, Phys. Rev. Lett. **102**, 226401 (2009).

[43] J. Heyd, G. E. Scuseria, and M. Ernzerhof, Hybrid functionals based on a screened Coulomb potential, J. Chem. Phys. **124**, 219906 (2006).

[44] S. Grimme, J. Antony, S. Ehrlich, and H. Krieg, A consistent and accurate ab initio parametrization of density functional dispersion correction (dft-d) for the 94 elements H-Pu, J. Chem. Phys. **132**, 154104 (2010).

[45] A. Fonari and S. Stauffer, vasp raman.py, https://github.com/raman-sc/VASP/ (2013).

[46] P. Bruesch, *Phonons: Theory and Experiments II* (Springer, Berlin, 1986).

[47] D. Porezag and M. R. Pederson, Infrared intensities and Raman-scattering activities within density-functional theory, Phys. Rev. B **54**, 7830 (1996).

[48] M. Lazzeri and F. Mauri, First-Principles Calculation of Vibrational Raman Spectra in Large Systems: Signature of Small Rings in Crystalline SiO_2, Phys. Rev. Lett. **90**, 036401 (2003).

[49] P. Umari, A. Pasquarello, and A. D. Corso, Raman scattering intensities in α-quartz: A first-principles investigation, Phys. Rev. B **63**, 094305 (2001).

[50] X. Gonze and C. Lee, Dynamical matrices, Born effective charges, dielectric permittivity tensors, and interatomic force constants from density-functional perturbation theory, Phys. Rev. B **55**, 10355 (1997).

[51] M. K. Niranjan, P. K. Kumari, K. Banerjee, and S. Asthana, Randomly arranged cation- ordered nanoregions in lead-free relaxor ferroelectric $K_{1/2}Bi_{1/2}TiO_3$: Prediction from first- principles study, J. Appl. Phys. **123**, 244106 (2018).

[52] M. K. Niranjan, Infrared reflectivity and Raman intensity spectrum of relaxor ferroelectric $Na_{1/2}Bi_{1/2}TiO_3$ at room temperature: A first-principles theoretical study, Mater. Res. Express **3**, 125501 (2016).

[53] See Supplemental Material at http://link.aps.org/supplemental/10.1103/PhysRevB.103.195437 for Tables S-1–S-5 and Figs. S-1 and S-2, which includes Refs. [67–71].

[54] J. Srour, M. Badawi, F. E. H. Hassan, and A. Postnikov, Comparative study of structural and electronic properties of GaSe and InSe Polytypes, J. Chem. Phys. **149**, 054106 (2018).

[55] L. Liang and V. Meunier, First-principles Raman spectra of MoS_2, WS_2 and their heterostructures, Nanoscale **6**, 5394 (2014).

[56] A. M-Sanchez and L. Wirtz, Phonons in single-layer and few-layer MoS_2 and WS_2, Phys. Rev. B **84**, 155413 (2011).

[57] G. Kern, G. Kresse, and J. Hafner, *Ab initio* calculation of the lattice dynamics and phase diagram of boron nitride, Phys. Rev. B **59**, 8551 (1999).

[58] G. Giovannetti, P. A. Khomyakov, G. Brocks, P. J. Kelly, and J. van den Brink, Substrate- induced band gap in graphene on hexagonal boron nitride: *Ab initio* density functional calculations, Phys. Rev. B **76**, 073103 (2007).

[59] E. Aulich, J. L. Brebner, and E. Mooser, Indirect energy gap in GaSe and GaS, Phys. Status Solidi B **31**, 129 (1969).

[60] R. Le Toullec, M. Balkanski, J. M. Besson, and A. Kuhn, Optical absorption edge of a new GaSe polytype, Phys. Lett. A **55**, 245 (1975).

[61] Y. Sun, S. Luo, X.-G. Zhao, K. Biswas, S.-L. Li, and L. Zhang, InSe: A two-dimensional material with strong interlayer coupling, Nanoscale **10**, 7991 (2018).

[62] V. Zolyomi, N. D. Drummond, and V. I. Fal'ko, Band structure and optical transitions in atomic layers of hexagonal gallium chalcogenides, Phys. Rev. B **87**, 195403 (2013).

[63] Ma Zhou, R. Zhang, J. Sun, W.-K. Lou, D. Zhang, W. Yang, and K. Chang, Multiband k·p theory of monolayer XSe (X = In, Ga), Phys. Rev. B **96**, 155430 (2017).

[64] L. Plucinski, R. L. Johnson, B. J. Kowalski, K. Kopalko, B. A. Orlowski, Z. D. Kovalyuk, and G. V. Lashkarev, Electronic band structure of GaSe(0001): Angle-resolved photoemission and *ab initio* theory, Phys. Rev. B **68**, 125304 (2003).

[65] P. C. Leung, G. Andermann, W. G. Spitzer, and C. A. Mead, Dielectric constants and infrared absorption of GaSe, J. Phys. Chem. Solids **27**, 849 (1966).

[66] N. M. Gasanly, A. Aydınlı, H. Özkan, and C. Kocabaş, Temperature-dependent Raman scattering spectra of ε-GaSe layered crystal, Mater. Res. Bull. **37**, 169 (2002).

[67] S. Benazeth, N. H. Dung, M. Guittard, and P. Laruelle, Refinement of the structure of the polytype 2H of a GaSe-β monocrystal, Acta Crystallogr., Sec. C **44**, 234 (1988).

[68] J. C. J. M. Terhell and R. M. A. Lieth, Preparation and crystallography of gallium sulfide- selenide solid solutions, Phys. Status Solidi A **5**, 719 (1971).

[69] V. M. Kaminskii, Z. D. Kovalyuk, M. N. Pyrlya, S. V. Gavrilyuk, and V. V. Netyaga, Properties of hydrogenated GaSe crystals, Inorg. Mater. **41**, 793 (2005).

[70] U. Schwarz, D. Olguin, A. Cantarero, M. Hanfland, and K. Syassen, Effect of pressure on the structural properties and electronic band structure of GaSe, Phys. Status Solidi B **244**, 244 (2007).

[71] C. De Blasi, D. Manno, and A. Rizzo, Convergent-beam electron diffraction study of melt- and vapour-grown single crystals of gallium chalcogenides, Nuovo Cimento D **11**, 1145 (1989).